Mechanical Properties of Atomic-Layer-Deposited Al$_2$O$_3$/Y$_2$O$_3$ Nanolaminate Films on Aluminum towards Protective Coatings

Janne-Petteri Niemelä,[1] Barbara Putz,[1,2]* Gustavo Mata-Osoro,[3] Carlos Guerra-Nuñez,[1†] Remo N. Widmer[1], Nadia Rohbeck,[1] Thomas E. J. Edwards,[1] Max Döbeli,[4] Krzysztof Maćkosz,[5,6] Aleksandra Szkudlarek,[5] Yury Kuzminykh,[3] Xavier Maeder[1], Johann Michler,[1] Bernhard Andreaus,[3] Ivo Utke[1]

[1] Laboratory for Mechanics of Materials and Nanostructures, Empa – Swiss Federal Laboratories for Materials Science and Technology, Feuerwerkerstrasse 39, Thun CH-3602, Switzerland.

[2] Department of Materials Science, Montanuniversität Leoben, Franz Josef Strasse 18, Leoben AT-8700, Austria.

[3] INFICON AG, Alte Landstrasse 6 9496 Balzers, Principality of Liechtenstein.

[4] ETH Zürich, Ion Beam Physics HPK H32, Otto-Stern-Weg 5, CH-8093, Zürich, Switzerland

[5] AGH University of Science and Technology, Academic Centre for Materials and Nanotechnology, av. Mickiewicza 30, 30-059 Krakow, Poland.

[6] AGH University of Science and Technology, Faculty of Physics and Applied Computer Science, av. Mickiewicza 30, 30-059 Krakow, Poland.

*Corresponding author (E-mail: barbara.putz@unileoben.ac.at)

ABSTRACT: Atomic layer deposition is an appealing deposition technology for the fabrication of protective coatings for various applications, including semiconductor manufacturing chambers and related metallic parts with complex 3D topographies, where a key requirement is (thermo) mechanical robustness of the coatings. Here we study the mechanical properties of atomic layer deposited Al_2O_3, Y_2O_3 and their nanolaminate coatings on Al metal substrate. Tensile straining experiments accompanied with in-situ optical and scanning electron microscopy indicate that the fragmentation onset of 100-nm thick coatings can be tailored in the strain range of 1.3 – 2.1 % by controlling the layer structure and composition of the nanolaminates, such that a higher Al_2O_3 content, denser layer spacing and amorphisation favor higher crack onset strain. Although the fracture toughness of Al_2O_3 and Y_2O_3 are found to be similar, $K_{IC} = 1.3$ MPa·m$^{1/2}$, the (substantially tensile) intrinsic residual stress for Y_2O_3 is a disadvantage for applications where tensile applied stresses are to be expected. The films adhere well to the Al substrate as significant delamination of the films is not observed in the tensile experiments; the analysis of the fragmentation patterns indicates that insertion of an Al_2O_3 layer at the film/substrate interface can enhance interface toughness. High-temperature (425 °C) tensile experiments for the Al_2O_3 films indicate good temperature tolerance for the coatings, and in comparison to the room-temperature data, a significant difference is seen in the increase of saturation crack spacing. Moreover, structure and composition of the films are studied in detail through X-ray reflection and diffraction, transmission electron microscopy, Rutherford backscattering spectrometry, and elastic recoil detection analysis. The results are particularly interesting for protective coating applications.

1. Introduction

Semiconductor manufacturing requires process steps involving conditions that are harsh and corrosive to the processing chamber and other related parts that often have complex three-dimensional topographies and are typically made of metals. To enhance the lifetime and the maintenance interval of these processing tools, protective coatings are required.[1, 2] The desired features for protective coatings include e.g. conformality of coatings over the complex tool topographies, compact pin-hole free nature, and plasma resistance. On top of these requirements, it is highly important that the coatings are sufficiently robust to withstand (thermally-induced) mechanical stresses at various temperatures. Materials of interest therefore include e.g. high-etch-resistance oxides, and for multi-property coatings, their nanolaminates and mixed oxides.

An appealing deposition technology for manufacturing of the protective coatings is atomic layer deposition (ALD),[3-9] in particular for its capability for reaching the deepest trenches and pores,[10] while delivering high-quality pinhole-free coatings.[11] These features stem from the unique way the coatings are built in an atomic layer-by-layer fashion by exposing the growth surface to precursor vapors in a cyclic manner, one precursor at the time.[11] The layer-by-layer nature of the technique moreover enables extremely good control over the layer thicknesses, which is particularly useful for designing (sub)nanoscale multilayer architectures. As now for the protection of semiconductor processing tools, these features have already made ALD films highly interesting for providing protection/passivation/encapsulation functionalities throughout a broad range of applications, including for instance batteries,[12, 13] solar cells,[14, 15] OLEDs,[16, 17] and medical instrument/implant coatings.[18, 19]

For the protection of semiconductor processing tools, the traditional protective oxide material Al_2O_3 has been largely replaced by Y_2O_3, a material with a substantially higher etch resistance in

fluorine-containing environments.[1, 2] While also combinations of these two materials are attractive from the perspective of (dry) etch resistance,[1, 2] they are particularly interesting for controlling the microstructure of the coatings and hence their mechanical characteristics. In our recent study, carried out for coatings deposited on polyimide substrates, we revealed that mixing Al_2O_3 and Y_2O_3 into nanolaminate structures provides us with an excellent means for controlling the fracture mechanical properties of these appealing protective coatings.[20] While the fracture mechanics of ceramic films prepared by methods such as physical vapor deposition and sol-gel deposition on metal substrates has received some attention,[21-23] the related literature on ALD films is limited to the investigations of the film properties on polymer surfaces.[20, 24-28] Apart from the here discussed application of chamber part protection, the enhanced mechanics understanding on the ALD films is relevant for applications where mechanical flexibility/stretchability is required, such as flexible (opto)electronics,[16, 17] flexible magnets[27] and tolerance of charge-discharge related volume changes in batteries,[26] while interfacing with metal surfaces is also required e.g. in the medical applications.[18, 19]

In this work, we study the fracture properties of Al_2O_3 and Y_2O_3 thin films and their nanolaminates, prepared on aluminum metal (Al6061-T6) substrates with the ALD technique. Aluminum is chosen because it is particularly application relevant. For example, many semiconductor manufacturing tools are Al-based: cheap, easy to manufacture, however, easily attacked by plasma gas processes. Enhancing their lifetime in harsh and corrosive environments is one of the target areas of our protective coatings. We demonstrate through uniaxial tensile testing coupled with in-situ optical and scanning electron microscopy that the relatively low critical strain for fracture of the Y_2O_3 coatings can be substantially enhanced through the nanolamination with Al_2O_3, such that a laminate structure with sub-nanometer layer thicknesses shows the best performance, beyond the rule-of-mixtures prediction. The onset for the film fracture is delayed on metal surfaces (in comparison to

polymer surfaces) presumably due to low yield strain of the substrate, a favorable finding for protective coating applications.

2. Experimental

2.1 Thin-film deposition

Thin-film coatings of Al_2O_3, Y_2O_3, and Al_2O_3/Y_2O_3 nanolaminates were prepared through ALD in a Picosun R-200 reactor. The deposition process was developed following a typical growth per cycle (GPC) saturation curve study. The depositions were carried out at a temperature of 300 ^oC from trimethyl aluminum (TMA; Epivalence), Tris(sec-butylcyclopentadienyl)Yttrium III ($Y(CpBu)_3$; Adeka) as the metal precursors and H_2O as the oxygen source. While TMA and H_2O were kept at room temperature, $Y(CpBu)_3$ was heated to 180 ^oC for sufficient volatility. Film thickness of ca. 100 nm was targeted. Four types of nanolaminates (NL1-NL4) were prepared with layer thickness patterns of $t_1+(t_2+t_3)n$, t_1 interfacing with the substrate (see also Table 1). Here t_1 and t_2 sum up to the thickness of the interface Al_2O_3 layer (IL), such that $t_1+t_2 \approx 14$ nm; to ensure constant metal-coating interface structure and comparability between the nanolaminates, t_3 refers to the Y_2O_3 deposit, and n is the number of bilayer repeats. For the NL1, NL2 and NL3 films the mean t_2 values were 14.8, 7.5 and 3.5 nm, respectively, while t_3 was kept constant at 6 nm. For NL4 t_2 and t_3 both were < 1 nm. The NL4 and the Y_2O_3 film were deposited with ($NL4_{IL}$ and Y_2O_{3IL}) and without the 14 nm Al_2O_3 interface layer (IL). A schematic of the different nanolaminate structures as well as the ALD deposition process is shown in Scheme 1. Silicon, Aluminum (Al6061-T6, 1 mm thickness, Goodfellow) and polyimide (50-µm-thick Kapton) substrates were coated in parallel in the same deposition run, the former for the structural characterization and the latter two for the tensile experiments. In-situ ozone treatment was applied for surface cleaning of the substrates prior to the ALD processing.
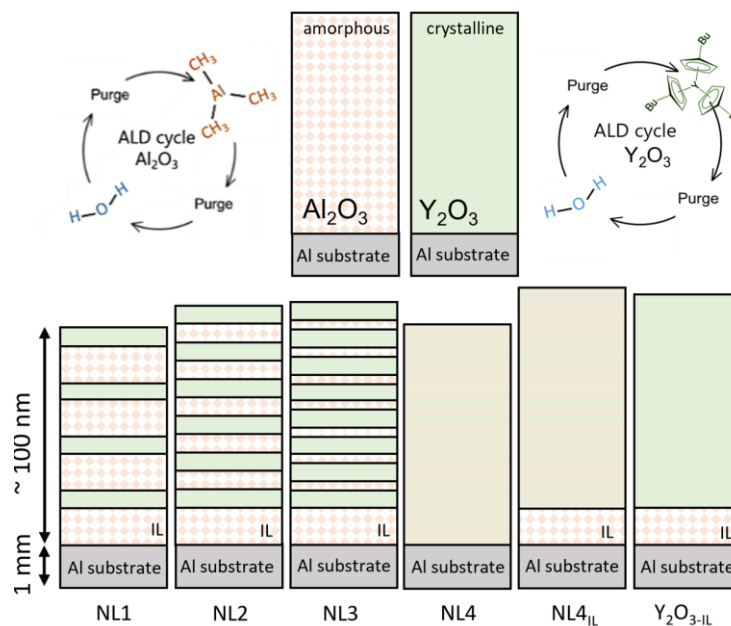
Scheme 1. Schematic of the different nanolaminate (NL) films on Al substrates as well as individual ALD cycles for the Al_2O_3 (left) and Y_2O_3 (right) constituents. Interface layers (IL) are indicated. Precise values for individual layer thicknesses are reported in Table 1.

Prior to the ALD coatings, the Al tensile specimens were prepared from larger (ca. 5×5 cm^2) Al plates as follows. First, the plates were polished such that the first polishing step was carried out with 1-um diamond grains, and as the second step to obtain mirror-like reflecting surface, polishing with 0.04-µm SiO_2 grains (MD–Chem, Struers) with OP-U lubricant was carried out. Finally, the substrates were laser patterned into the so-called dogbone shapes with a 3-mm long gauge section (see Figure S1 for more details on the geometry) specifically fit for the tensile straining experiments. Four tensile specimens were simultaneously coated in each ALD run.

2.2 Structural characterization

The elemental composition of the films was measured with Rutherford backscattering spectrometry (RBS; 2 MeV He ions), together with He-based Elastic Recoil Detection (ERD), and 13 MeV ^{127}I Heavy Ion Time-of-Flight Elastic Recoil Detection Analysis (ToF-ERDA). Thickness, density and

roughness of the films were obtained by using the X-ray reflectivity (XRR, Bruker D8 Discover) technique for the films deposited on silicon substrates. The incident beam (Cu Kα) was conditioned by a Göbel mirror, a 0.1° divergence slit and a 0.1° anti-scatter slit. The measurements were done in θ-2θ geometry over the 2θ range of 0.1-2.5° and the reflectivity patterns were analyzed by fitting the data to a physical model using DIFFRAC LEPTOS (Bruker) software. The fitting model was sensitive to all fitting parameters. Based on a detailed analysis for the NL1 film, for thickness and roughness a deviation of 10 % from the best-fit values lead to > 500 % and > 67 % increase in the goodness-of-fit value (chi square; the smaller the value the better the fit), respectively. Lower sensitivity was found for roughness, such that 40 % deviation from the best-fit value lead to 5 % increase in the goodness-of-fit value. The crystallinity of the thin films was investigated by the grazing incidence X-ray diffraction (GIXRD) technique (Bruker D8 Discover diffractometer). The diffractometer was operated at a fixed angle of incidence of 0.5° using CuK_{α} (λ=1.5418 Å) radiation, scanning the 2θ angle in the range of 15°-70°. The incident beam was conditioned with a Göbel mirror and a 0.6 mm slit, while the diffracted beam was passed through an equatorial soller slit, 0.0125 mm Ni filter and 9.5 mm slit to a 0D detector. The scan was carried out in steps of 0.02°and the measurement time for each step was 2 s.

The lamellae for transmission electron microscopy (TEM) were prepared for selected samples using a TESCAN Lyra gallium focused ion beam scanning electron microscope (FIB/SEM). A protective layer of Pt-C nanocomposite was deposited from the $MeCpPtMe_3$ precursor, first using an electron beam (30 keV, 500 pA) and then using a Ga^+ ion beam (30 keV, 100 pA). Then the standard protocol was applied for the lift-out process and the attachment to the TEM grid. The final thinning was carried out using 30 keV and 30 pA to obtain the lamella thickness below 100 nm without the last conventional polishing steps. TEM lamellas were characterized by using an aberration-corrected TEM from Thermo Fisher – a Titan Themis 200 equipped with a high-

brightness X-FEG electron source. The cross-sectional analyzes were performed at 200 kV by high-resolution TEM (HR-TEM) with convergent beam screen current of 4 nA and high-resolution scanning TEM (HR-STEM) with a screen current of 35 pA.

2.3 Mechanical characterization

The Young's moduli of the Al_2O_3 (180 GPa) and Y_2O_3 (184 GPa) films deposited on Si substrates were determined using fully elastic nanoindentation with a spherical indenter on a ZHN Nanoindenter (ZwickRoell).[29] Squares of approximately 4 mm × 4 mm of each sample were glued onto steel sample holders using heated rosin. The spherical indenter had an average radius of approximately 6.6 μm, as determined from radius function fitting based on purely elastic reference measurements in fused silica and sapphire single crystal. A constant load of 20 mN was chosen for all measurements. 50 individual force-displacement curves were averaged per sample. The Young's moduli of the films were refined by fitting a calculated indentation curve to the experimental indentation curve. The analytical curve is calculated using a model based on Hertzian contact theory for a bilayer system, as implemented in the ZHN software. The constant input parameters included the Young's modulus of the substrate (165 GPa; measured in-house with the same method), the Poisson's ratio of the substrate (0.22), the film thicknesses (~ 100 nm; Table 1) and the Poisson's ratio of the films (0.24 for Al_2O_3[30] and 0.3 for Y_2O_3[31]). Both films were measured twice (two squares, the same deposition run). The estimated error of the averaged Young's moduli is approximately 25 GPa. The elastic moduli of the NL1-NL4 were obtained through the rule-of-mixtures prediction for two-component multilayer materials through the Reuss formula (cross-plane)[32]

$$1/E = f_1/E_1 + f_2/E_2, \tag{1}$$

where f represents volume fraction, E is elastic modulus, and the indices 1 and 2 refer to the values for the Al_2O_3 and Y_2O_3 single-layer thin films.

The residual stress values for the films deposited on Si wafers were obtained through the wafer bow method (FSM 500TC). In order to derive the corresponding values on the Al substrate, the residual stress is first decomposed into its intrinsic (σ_i) and thermal components ($\sigma_{\Delta T}$) as

$$\sigma_r = \sigma_i + \sigma_{\Delta T}. \tag{2}$$

The thermal component captures the effect of cooling down (ΔT) from the deposition temperature of 300 °C to room temperature (25 °C) and is written as[30]

$$\sigma_{\Delta T} = E(1-v)^{-1}(\alpha_s - \alpha)\Delta T. \tag{3}$$

Here, E, v and α are the elastic modulus, Poisson's ratio and thermal expansion coefficient of the film, respectively, while α_s is the thermal expansion coefficient of the substrate. Through writing and combining equations (2) and (3) for the Al and Si substrates, and assuming that σ_i is substrate independent, one arrives at

$$\sigma_r^{Al} = \sigma_r^{Si} + E(1-v)^{-1}(\alpha_s^{Al} - \alpha_s^{Si})\Delta T, \tag{4}$$

which was used to calculate the residual stress values for the films on the Al substrate. The respective elastic strains (ε_r, ε_i and $\varepsilon_{\Delta T}$) were obtained by dividing the stress values (in equations 2-4) by E/(1-v). Rule-of-mixture approximations (originally for fiber composites) were used to evaluate the in-plane Poisson's ratio (v)[33] and the linear thermal expansion coefficient (α)[34] for the nanolaminates NL1-NL4:

$$v = f_1 v_1 + f_2 v_2 \tag{5}$$

$$\alpha = (E_1\alpha_1 f_1 + E_2\alpha_2 f_2)/(E_1 f_1 + E_2 f_2). \tag{6}$$

The thin films deposited on the metal substrates were characterized through uniaxial tensile straining experiments. They were carried out using a tensile stage (MTI 8000-0010) equipped with a digital optical microscope (Keyence 500F) or a scanning electron microscope (SEM; Tescan Mira) for in-situ monitoring of the fragmentation process. For the optical monitoring the tensile stage was operated continuously at a constant strain rate of 2×10^{-4} s^{-1} by means of displacement control, and microscope images were recorded at strain intervals of 2×10^{-4} (i.e. 1 per second) for subsequent analysis. For the in-situ SEM monitoring the straining was stopped at appropriate strain steps and the sample surface was imaged (operation voltage: 5 kV). Four tensile samples per ALD condition were analyzed to assess the statistical fluctuations in the results. The strain values were determined via digital image correlation by tracking the distance between features on the sample surface. For high temperature experiments, a heating bar (Bach RC) was incorporated in the tensile stage such that it provided near-contact heating below the dogbone. Temperature was calibrated through reference measurements with a K-type thermocouple spot welded to the top of the gauge section of the dogbone. The ends of the dogbone were not gripped during the temperature ramp up so that the sample was able to expand freely; therefore tensile thermal strain was generated in the films due thermal expansion coefficient mismatch between the film and the substrate.

The yield strain of Al was obtained by dividing the yield stress of 0.260 GPa by the elastic modulus of 70 GPa (datasheet Aluminum 6061T6 Goodfellow). Thermal expansion coefficient of Al was also taken from the data sheet (6061T6 Goodfellow). The yield strain for polyimide was taken from the datasheet (DuPont™ Kapton® HN).

3. Results and discussion

3.1 Structural properties

The XRR technique was employed for characterization of the layer structure, density and roughness of the thin films deposited on Si substrates (Figure 1a,b). The XRR patterns show the following features: a plateau of total reflection for 2θ values below the critical angle at ca. 0.5°, followed by a rapid decrease of the reflected intensity and formation of distinctive fringe patterns. The single layer Al_2O_3 and Y_2O_3 films exhibit patterns with small fringes that stem from the interference from the substrate-film and film-air interfaces, and hence relate to the total film thickness. The NL1-NL4 films exhibit, in addition to the small fringes, the large fringes that correspond to the interference from the internal Al_2O_3/Y_2O_3 interfaces, and hence relate to the individual layer thickness in the multilayer stack. The NL4 film shows, due to its low bilayer thickness, only one multilayer fringe in the 2θ range of 0.1-10°, which peaks out from the noise region of the pattern (Figure 1b).

Thickness values for the film and layer thicknesses obtained from fitting of the XRR patterns are compiled in Table 1. For the NL4 film the reflection at $2\theta = 8.9°$ translates (through the Bragg law) to a bilayer thickness of 0.99 nm. The density values for the single-layer Al_2O_3 and Y_2O_3 films are 3.1 and 4.9 g/cm^3, being below the respective full-density value of 3.95 g/cm^3 for Al_2O_3 (based on
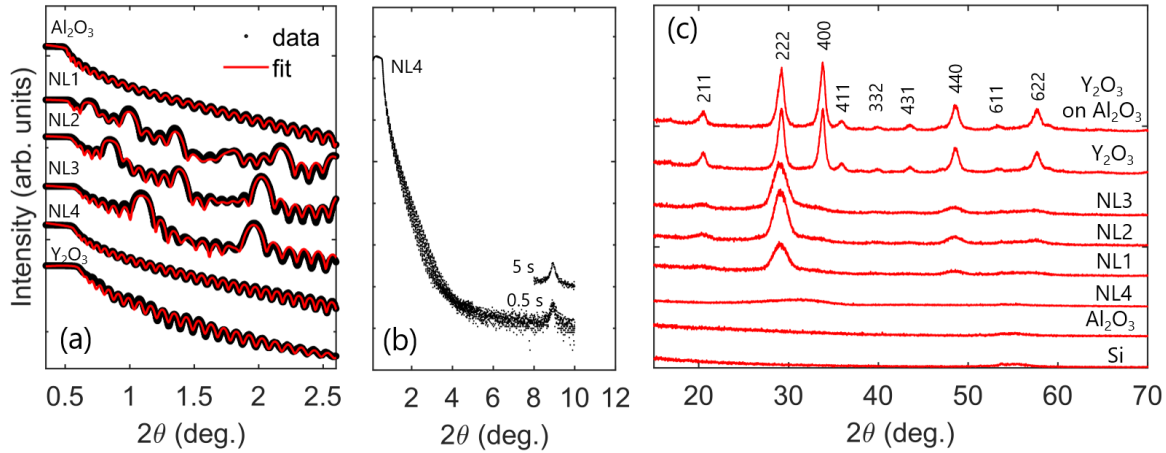
Figure 1. (a) X-ray reflection patterns together with the respective fits. (b) The pattern for the NL4 as measured in a wider 2θ range of 0.1-10 deg. with accumulation time of 0.5 s per step and in the narrow range of 8-10 deg. with accumulation time of 5s. (c) Grazing incidence X-ray diffraction patterns; the Miller indices for the Y_2O_3 structure were retrieved from the ICDDPDF41-1105 card.

the lattice constants of the hexagonal α-Al_2O_3 structure)[35] and very close to the full-density value of 5.04 g/cm^3 for Y_2O_3 (based on the lattice constants of the cubic structure).[36] This is reasonable as our Al_2O_3 is amorphous and Y_2O_3 is well crystalline (Figure 1c), and is in line with the previously reported data in the literature (Table 1).[37-42] The value for Al_2O_3 falls in the upper end of the range of 2.1-3.6 g/cm^2 expected for amorphous Al_2O_3;[43] the reasonably high density for our amorphous Al_2O_3 is in line with the low impurity content observed (later in the chapter). The mean density values (thickness-weighted average over the density values for individual Al_2O_3 and Y_2O_3 layers) for the nanolaminate films expectedly increase with increasing Y_2O_3 content in the films, a fact that is also seen in the increase of the critical angle of the XRR patterns (Figure 1a). All the

films are smooth with surface roughness around 1 nm, with the nanolaminate films having slightly lower roughness than the single-layer films.

The GIXRD technique was used to study the crystallinity of the films (Figure 1c). The Al_2O_3 film was found to be amorphous which is typical for Al_2O_3 fabricated through the TMA/H_2O process, while the Y_2O_3 film crystallized in the cubic crystal structure (*Ia3*). The Y_2O_3 layers in the NL1, NL2 and NL3 crystallized with the same cubic structure as the single-layer Y_2O_3 film, with the difference that substantial peak broadening is seen for the nanolaminates. The FWHM is around 1.8° for all the laminates, which translates to the average grain-size approximate of 4.6 nm through the Scherrer formula for the 222 reflection. This is reasonable as the layer thickness for the individual Y_2O_3 layers is known to be around 6 nm from the XRR experiments, and therefore, the Y_2O_3 layers are, in the least, nearly fully crystalline in the NL1-NL3 films. The GIXRD pattern for the NL4 with a broad feature around 32° suggests presence of very small nanocrystals/near amorphous structure for Y_2O_3 layers of thickness on the order of 0.5 nm only. Moreover, even though the grazing incidence measurements do not directly give information on grain orientation (with respect to the substrate normal), the absence of the 222 Y_2O_3 peak for the nanolaminates most likely indicates change in the texture of the films.

Table 1. Thickness, density and roughness from the X-ray reflection analysis for the films deposited on the Si substrates. The mean values refer to the values in the repeated bilayer unit in the nanolaminates. $NL4_{IL}$ and Y_2O_{3IL} refer to the samples with the Al_2O_3 interface layer inserted. For fitting sensitivities, see Experimental.

	Al_2O_3	NL1	NL2	NL3	NL4	$NL4_{IL}$	Y_2O_3	Y_2O_{3IL}
Total thickness (nm)	94	83	88	85	100	98	84	106
Al_2O_3 thickness interface ($t_{1+}t_2$; nm)	-	14.2	14.3	12.9	-	14.9	-	13.5
NL Al_2O_3 thickness mean (t_2; nm)	-	14.8	7.5	3.5	-	-	-	-
NL Y_2O_3 thickness mean (t_3; nm)	-	5.8	6.1	5.9	-	-	-	-
Mean density (g/cm^3)	3.1	3.5	3.8	4.1	4.0	4.2*	4.9	4.9*
Al_2O_3 density interface (g/cm^3)	-	2.9	3.1	3.0	-	3.0	-	3.2
NL Al_2O_3 density mean (g/cm^3)	-	2.9	3.0	3.0	-	-	-	-
NL Y_2O_3 density mean (g/cm^3)	-	4.9	4.9	4.9	-	-	-	-
Surface roughness (nm)	1.0	0.9	0.9	0.8	0.6	0.7	1.0	1.3

* Excluding the density of the Al_2O_3 interface layer.

The TEM studies confirmed the layer structures analyzed in detail through the XRR technique (Figure 2); for the NL1 film (Figures 2a and 2b), measurement of layer thicknesses along a vertical line yields average thickness values of 14.4 nm and 6.0 nm for the Al_2O_3 and Y_2O_3 layers, respectively, well in line with the XRR data (Table 1). Remarkably, HAADF-STEM imaging can visualize the *sub-nm* multilayer character for the NL4 film (Figure 2c); based on the taken electron diffraction pattern the NL4 film is near amorphous (Figure S2). For the NL1 film TEM indicates that the Y_2O_3 layers are fully crystalline (Figure 2a,b), in line with GIXRD data (Figure 1c). The

HR-TEM image in Figure 2b also indicates that the interfaces between Y_2O_3 and Al_2O_3 sublayers are distinct, dense, and homogeneous.
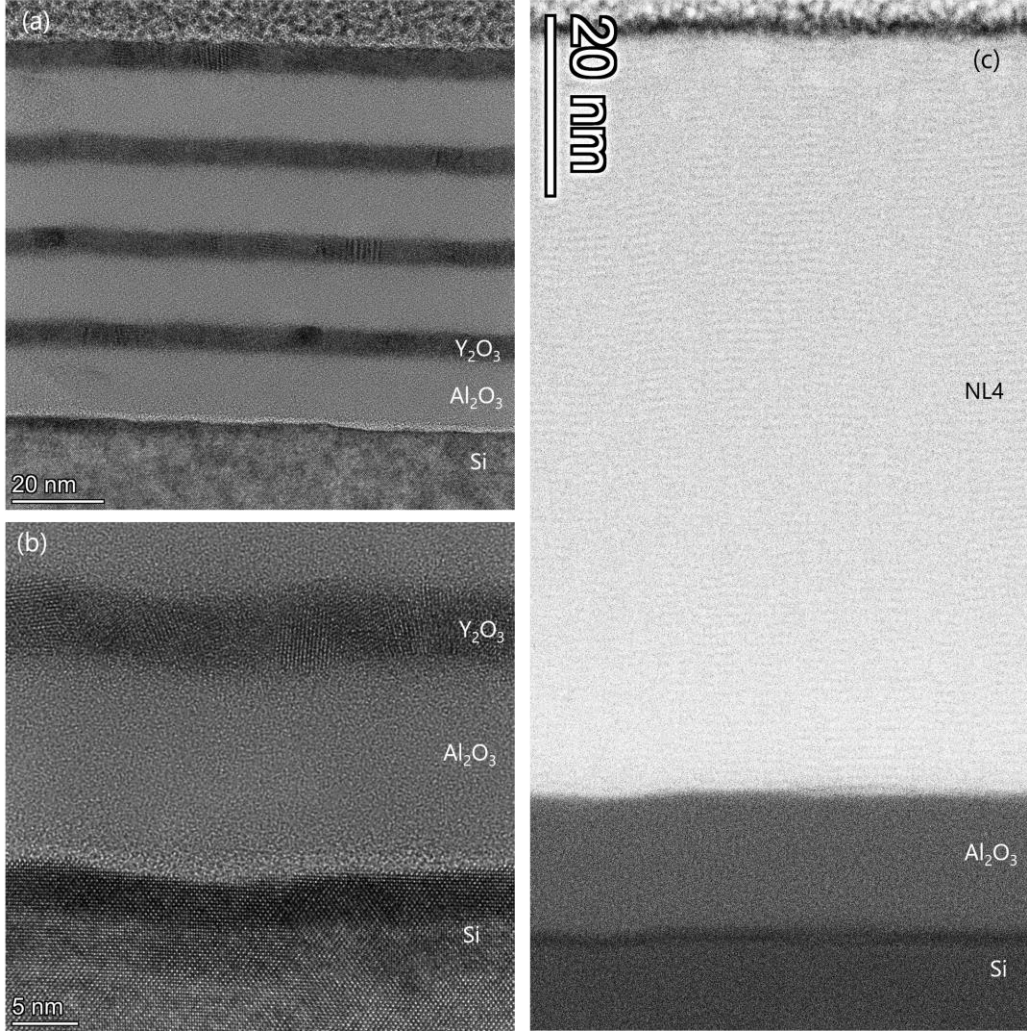
Figure 2. (a) Transmission electron microscope (TEM) and (b) High resolution (HR) TEM images of the NL1 film on Si substrate, and (c) High-angle annular dark-field scanning transmission electron microscopy (HAADF-STEM) image of the NL4 film on Si substrate. The thin layer between the Si substrate and Al_2O_3 is the native SiO_x. Note that in TEM higher mass density is seen in dark, while in HAADF-STEM higher density corresponds to light tone.

The composition of the films was studied through Rutherford Backscattering Spectrometry (RBS) and Time-of-Flight Elastic Recoil Detection Analysis (ToF-ERDA). The aluminum oxide film is stoichiometric $Al_2O_{3+\delta}$ within the measurement accuracy of $\delta = \pm 0.12$. The number density of atoms per surface area (N/A) was extracted from the RBS data as 9.5×10^{17} cm^{-2}, which translates to deposition of 3.8×10^{14} Al atoms per cm^2 per ALD (half) cycle, in accordance with the previous

15

observations in the literature for the deposition temperature of 300 $^{\circ}$C.[37] The impurity contents for the Al_2O_3 film are low: H ~ 1 at.% and C < 0.5 at.% in the bulk of the film. The yttrium oxide film is stoichiometric $Y_2O_{3+\delta}$ within the measurement accuracy of $\delta = \pm 0.15$. The number density of atoms per surface area (N/A) is 5.4×10^{17} cm^{-2}, which translates to deposition of 3.7×10^{14} Y atoms per cm^2 per ALD (half) cycle. The fact that this number is lower than that for Al_2O_3, can be ascribed to the larger ionic radius of Y with respect to that for Al, and perhaps partly to the slightly higher impurity levels for C and H of 1.4 at.% and 3.4 at.%, respectively. The atomic fractions for the NL4 are Y:Al:O = 0.75:1.24:3 implying that the composition follows the stoichiometry of yttrium aluminum garnet (YAG; $Y_3Al_5O_{12}$), despite the layered characteristics. The number density of atoms per surface area (N/A) for the NL4 is 8.2×10^{17} at/cm^2, which translates to deposition of 2.7×10^{14} metal atoms per cm^2 per ALD (half) cycle on average (Al or Y), and the comparison to the single layer films thus implies nucleation delay effects. Similar to the Al_2O_3 films, the NL1-NL4 films show low impurity levels of H ~ 1 at.% and C < 0.5 at.% in the bulk of the film.

3.2 Crack Onset Strain and Fracture Toughness

Mechanical fracture properties of the films were studied via uniaxial tensile testing coupled with in-situ optical and electron microscopy for the films deposited on the dogbone-shaped Al substrates. The samples were strained without any visual changes in the film morphology until the observation of the first crack (of finite length), perpendicular to the straining axis, at the crack onset strain (COS; Figures 3a,b). Further increase in tensile strain leads to formation of more and more cracks (and increase in their length) until the fragmentation process finally saturates (Figures 3c,d). We note that there was a good agreement between the COS values from the continuous optical and the interrupted SEM experiments (Figure S3), and therefore, values from both the methods were used in the calculation of the average COS. Cross-sectional TEM investigation shows that the

16

cracks penetrate through the full thickness of the coating, but do not propagate into the Al substrate (Figures 3e and 3f); this contrasts to what has been seen e.g. for polyethylene terephthalate substrates.[44] The horizontal crack opening is seen to increase with increasing tensile strain; where the substrate surface is no longer constrained by the coating, the deformation of the substrate normal to the surface is facilitated, and the sample surface now offsets in the vertical direction between crack faces (Figure 3f). Stress concentration and deformation of the substrate in the vicinity of a crack has also been observed for other film-substrate ((Cu/W)/Kapton) systems in the literature.[45]

The Al_2O_3 film exhibits a higher COS value (1.84 %) than the Y_2O_3 film (1.38 %), while the data for the nanolaminates demonstrates that the inclusion of the Al_2O_3 layers in the films provides us with an efficient means for enhancing the COS values with respect to Y_2O_3 (Figure 4a). With some scattering in data, the COS values scale roughly with the volume fraction of Al_2O_3 in the films. The COS values for the Y_2O_3 film and for the NL4 film indicate that the addition of the Al_2O_3 interface layer is effective for further delaying the onset of the fragmentation process. It stands out from the data that NL4 with the Al_2O_3 interface layer shows performance (COS = 2.05 %) that is superior even to the Al_2O_3 single layer film. While mechanically speaking a high COS is favorable it is essential to also keep in mind the evolution of etch rate and corrosion resistance for substrate protection and longevity of the coatings. In this regard it has been shown that Y_2O_3 is more corrosion resistant against plasma and adding more Al_2O_3 will reduce the corrosion resistance. [2] Therefore, the presented COS evolution can serve as a guideline to help find an acceptable balance between mechanical performance and corrosion resistance.
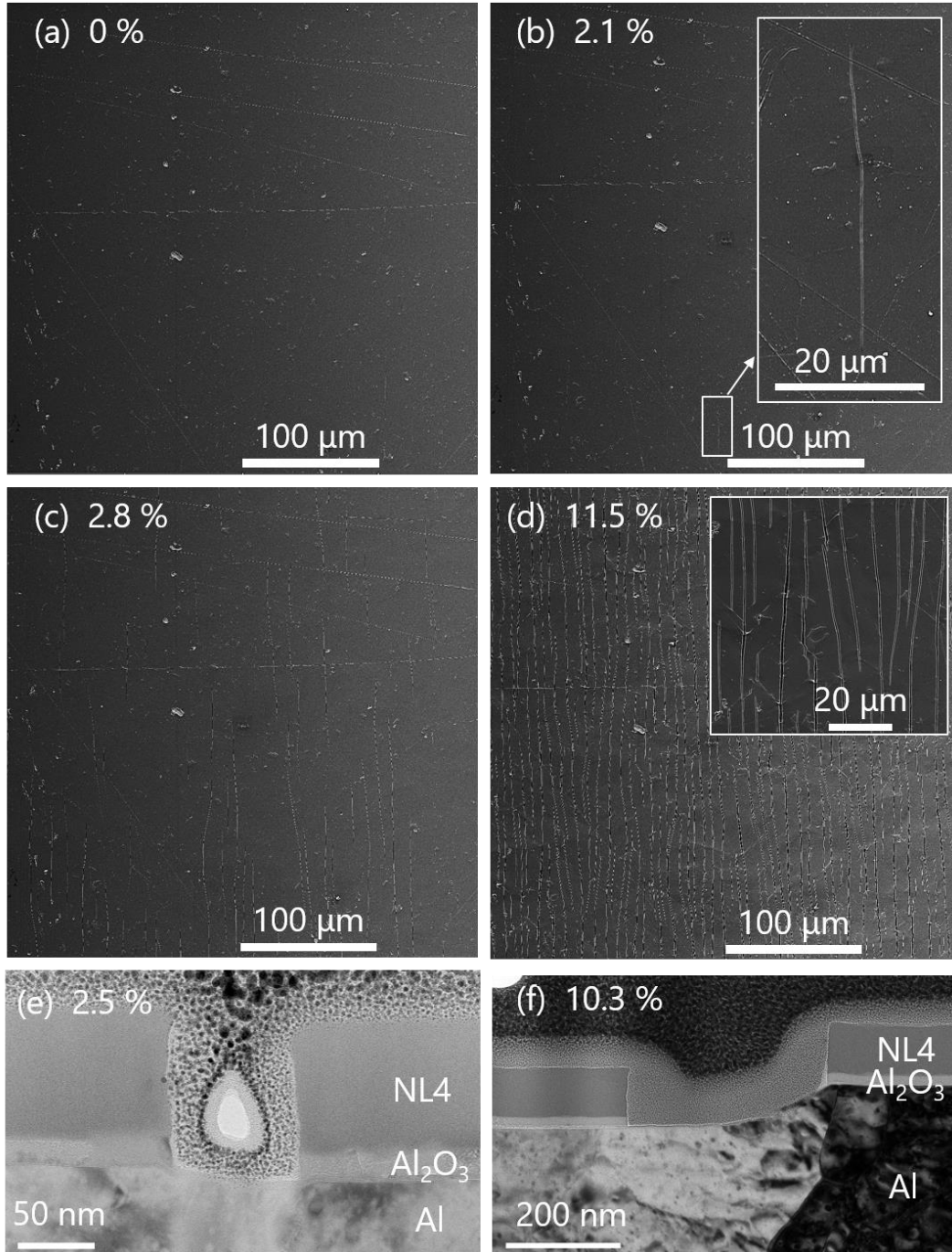
Figure 3. Top-view SEM images of the surface of the NL4 film on Al_2O_3 interlayer (on Al substrate) at different tensile strain states: (a) 0 %, (b) 2.1 % with onset of the cracking depicted, (c) 2.8 % with fragmentation evolving, and (d) 11.5 % with saturation of the crack spacing reached. The insets in (b) and (d) show higher magnification images of the film surface. Randomly oriented lines, already visible at 0% in (a), are scratches on the metal surface below the ALD film, introduced during substrate polishing. Cross-section TEM images in the vicinity of a crack at strain states of (e) 2.5 % and (f) 10.5 %; the material on the top of the NL4 film and in the crack is the local Pt-C protection layer applied prior to lamella preparation. Tensile strain acts in the horizontal direction in the images, i.e. perpendicular to the cracks.
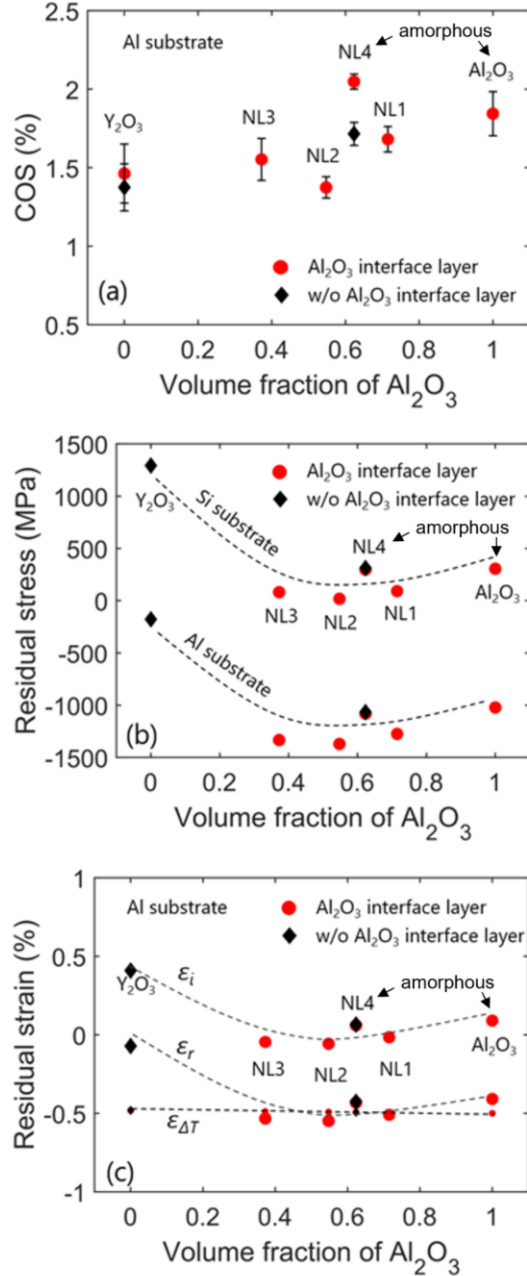
Figure 4. (a) Crack onset strain (COS) for the films on Al substrate, from the tensile straining experiments at room temperature; the error bars represent standard deviation over 3-4 measurements. (b) Residual stress of the films grown at 300 °C on Si from the Si wafer curvature measurements at room temperature, and for the Al substrate, as converted through equations (2-4). (c) Room-temperature residual strain ($\varepsilon_r = \varepsilon_i + \varepsilon_{\Delta T}$; ε_i is intrinsic strain, $\varepsilon_{\Delta T}$ is thermal strain for cooling to room temperature from 300 °C) of the films on Al, as obtained through equations (2-4). For the NL1-NL3 the volume fractions are based on layer thicknesses from the XRR measurements, and for the NL4 on the elemental Y/(Y+Al) fraction from the RBS measurements. The additional thicknesses in the Al$_2$O$_3$ interface layers do not count towards the volume fractions. The positive and negative signs for stress and strain signify tensile and compressive states, respectively. Dashed lines serve as guides to the eye.

The COS values may be influenced by the residual stress built up in the films during their deposition; therefore, the residual stress was evaluated through the Si wafer curvature method (at room temperature). As the thermal expansion coefficients for the film materials (α_{Al2O3} = 4.2×10^{-6} K^{-1} and α_{Y2O3} = 6.7×10^{-6} K^{-1})[30, 36, 46] are higher than that for Si ($\alpha_s{}^{Si}$ = 3.0×10^{-6} K^{-1})[30], it follows from equation (2) and (3) that for the films deposited on Si substrates tensile stress is expected upon post-deposition cooling (when the thermal component dominates in equation (2)). Indeed, all our films exhibit tensile residual stress on Si such that the measured stress value for the crystalline Y_2O_3 is clearly the highest (1293 MPa), while the amorphous Al_2O_3 exhibits notably lower stress value of around 300 MPa (Figure 4b). The multilayer engineering allows for further stress relief with values clearly below 100 MPa for the NL1-NL3, although any clear trends with the composition are not observed. Stress relief could be due to reduced layer thicknesses of the individual layers in the nanolaminates. The NL4 film (with and without the Al_2O_3 interlayer) shows values similar to that for Al_2O_3, perhaps due to the sub-nm layer thicknesses in NL4 that bring it closer to a state of mixed oxide of near amorphous character.

In contrast to Si, the thermal expansion coefficient for Al (23×10^{-6} K^{-1} for Al6061-T6, datasheet) is notably higher than those for our film materials, and therefore, compressive stress/strain (estimated through equation (4)) develops upon post-deposition cooling in the films deposited on the Al substrates (Figures 4b and 4c). The values closely follow the pattern for the films on Si, now with the negative sign, such that a residual strain value down to around -0.55 % is achieved for the NL2 (Figure 4c). We notice that the sample-to-sample trends in the total residual strain are governed by the intrinsic component that is notably tensile for Y_2O_3 (0.41 %) and closer to zero for the other samples (-0.06 to +0.09 %). The thermal component is the main driver for the substantially compressive nature of the residual strain. Compressive strain is beneficial for tolerance of externally applied tensile strain and acts as an initial offset to overcome in our (room-

temperature) tensile experiments. Therefore, if the COS values from our tensile experiments were only driven by the residual stresses, one would expect the NL2 film to have the highest COS value. As however the COS values for the NL4 and Al_2O_3 are clearly higher than that for NL2, the champion performances of NL4 and Al_2O_3 can likely be explained by the (near) amorphous character of these films, and nanocrystalline-to-amorphous transition thus seems to dominate here over the residual stress for the best COS performance.

As the NL4 film with the Al_2O_3 interface layer has a higher COS value than NL4 without interface layer but their residual stress/strain values are virtually the same, the Al_2O_3 interface layer must act through a route unrelated to the residual stress. It is hypothesized that the Al_2O_3 interface layer helps to form a higher quality interface with the native Al_2O_3 on our Al substrate, with less defects to trigger crack initiation and propagation. This is feasible as we observe Al_2O_3 interface layer to enhance film-substrate interface toughness (Chapter 3.3). Another parameter influencing COS and crack propagation is surface roughness.[47] The NL4 films exhibit the lowest roughness value in the series (as measured on Si; Table 1), potentially promoting a higher COS value. However, the fact that surface roughness values for the NL4 films with and without the Al_2O_3 interface layer are almost the same, identifies the interlayer as a major contributor. To be clear, the comparison of COS values of NL4 with and without Al_2O_3 interlayer (Figure 4a) shows that having an interlayer can be beneficial. It is possible that further improvements could be achieved through a detailed optimization of the interlayer thickness. However, rather than identifying the optimal interlayer thickness the main goal here was to ensure identical interface configuration allowing comparison between our different nanolaminates.

The COS values observed in the present work for the films deposited on the Al metal substrates (COS up to ~ 2 %) seem higher than the values typically reported for oxide films (of ~ 100 nm thickness) on polymer substrates (COS up to ~ 1 %).[20, 24, 27, 48] To study the effect of the substrate

on the COS values, we performed additional room-temperature tensile experiments for the Y_2O_3 film (the poorest performance on Al) and the NL4 film with the Al_2O_3 interlayer (the champion performance on Al) on polyimide substrates (see Figure S4 for example microscope images). Indeed, the COS values were clearly lower for the coatings on polyimide than for the same coatings on Al substrates: 0.83±0.04 % (polyimide) vs. 1.38±0.15 % (Al) for Y_2O_3 and 1.08±0.06 % (polyimide) vs. 2.05±0.05 % (Al) for the NL4 film with the Al_2O_3 interlayer. As the thermal expansion coefficient for polyimide (20×10^{-6} K^{-1}; datasheet) is close to that for Al (23.3×10^{-6} K^{-1}; datasheet), the substrate-induced difference in the thermal strain related to the post-deposition cooling is small ($\varepsilon_{\Delta T}^{Al}$ - $\varepsilon_{\Delta T}^{polyimide}$ = 0.1%) and cannot explain the differences in the COS values. An evident difference between Al and polyimide from the mechanical perspective is the magnitude of the yield strain; while the yield strain for Kapton is 3 %, the respective value for our Al is only 0.37 %. This means that when the fragmentation process of the coatings onsets, the Al substrate is already strained to the plastic regime, while polyimide is still deforming elastically. As at the same time it is known that plasticity in the substrate hampers stress transfer from the substrate to the film, and therefore delays the onset of cracking,[49] we ascribe the relatively large COS values observed here for the films on Al substrate to the small yield strain of Al. Moreover, elastic mismatch between the film and the substrate decreases going from the polyimide to the Al substrate, which together with the yielding (typically localized in specific grains) of the Al substrate, decreases the likelihood of the crack propagation.[50] In this respect we note that we observe slower propagation of the crack fronts across the film surface (perpendicular to the straining axis) for the films on Al in comparison to that for those on polyimide, as is qualitatively evident from comparison of Figure 3c and Figure S4c. Moreover, as improved adhesion regularly results in higher COS values,[51, 52] it is conceivable that the excellent adhesion of Al_2O_3 to Al (as the natural oxide) further promotes the higher COS values on Al.

The resistance of a material to the crack propagation at the onset of the fragmentation process can be further quantified in terms of (mode I) fracture toughness

$$K_{IC} = (E^*\text{COS} + \sigma_r^{Al}) \left(\frac{E\pi hg}{2E^*}\right)^{1/2},$$ (7)

where $E^* = E/(1-v^2)$ is the effective elastic modulus of the film and h is the film thickness.[50] In the stress term E^*COS represents the applied stress at the onset of the fragmentation process as obtained through digital image correlation, and σ_r^{Al} is the residual stress on Al at room temperature as obtained through equations (2-4). As the influence of the residual strain is implicit in the experimental COS value, the fracture stress E^*COS $+ \sigma_r^{Al}$ represents the tensile stress felt by the faces of a channeling crack, the actual driver for the channeling process. The elastic mismatch between the substrate (s) and the film is accounted for by the factor $g = g(D_1, D_2)$, where $D_1 = (E^* - E_s^*)/(E^* + E_s^*)$ and $D_2 = D_2(E^*, E_s^*)$ are Dundur's parameters, such that g increases with increasing elastic mismatch ($E^*-E_s^*$).[50]

Our films exhibit K_{IC} values in the range of 0.61-1.41 MPa·m$^{1/2}$, the NL4 with the Al$_2$O$_3$ interlayer showing the highest value (Table 2). As the elastic modulus values for our films are nearly equal (180-184 GPa), the changes in the g-factor are negligible, and the changes in K_{IC} are dominated by balancing of the COS and the residual stress effects in the stress term of equation (7). The notable difference between the COS (property of the film-substrate pair) and K_{IC} (property of the film material only) trends is that the K_{IC} values of Al$_2$O$_3$ and Y$_2$O$_3$ are virtually equal, i.e., Al$_2$O$_3$ and Y$_2$O$_3$ are equally tough as materials to resist fracture. The drawback for Y$_2$O$_3$ is therefore the large tensile intrinsic stress component that weakens its performance under applied tensile stress. The K_{IC} value of 1.3 MPa·m$^{1/2}$ for our Al$_2$O$_3$ film falls in the range (1.3-2.2 MPa·m$^{1/2}$) reported previously for ALD Al$_2$O$_3$ films on polymer substrates;[20, 24] this is plausible as our higher COS

value (due to the early onset of plasticity in Al) in the stress term, is compensated for by the lower

g value (higher elastic modulus of Al).

Table 2. Mechanical parameters for the film materials related to the fracture toughness and interface toughness calculations: fracture stress (E^*COS$+\sigma_r^{Al}$), crack onset strain (COS), thermal stress on Al substrate (σ_T^{Al}), intrinsic stress (σ_i), the g-factor,[50] fracture toughness (K_{IC}), strain for crack count saturation (ε_{sat}) and the lower bound film-substrate interface toughness (Γ_{if}). Elastic modulus, Poisson's ratio and thermal expansion coefficient are listed in Table S1. The error in COS and K_{IC} represent the standard deviation over four tensile experiments. The error in Γ_{if} is estimated as 15 % from comparison of different data treatment and analysis methods.

Sample	E^*COS$+\sigma_r^{Al}$ (GPa)	COS (%)	σ_T^{Al} (GPa)	σ_i (GPa)	g	K_{IC} (MPa·m$^{1/2}$)	ε_{sat} (%)	Γ_{if} (J/m^2)
Al$_2$O$_3$	2.51	1.84±0.14	-1.25	0.23	1.84	1.27±0.14	6.4	30±5
NL1	2.00	1.68±0.08	-1.24	-0.04	1.85	0.95±0.08	7.1	33±5
NL2	1.33	1.37±0.07	-1.23	-0.14	1.86	0.65±0.07	8.7	53±8
NL3	1.75	1.55±0.13	-1.22	-0.11	1.86	0.84±0.13	8.3	47±7
NL4	2.29	1.72±0.07	-1.23	0.17	1.86	1.19±0.08	5.9	27±4
NL4$_{IL}$	2.92	2.05±0.05	-1.23	0.15	1.86	1.51±0.05	7.3	42±6
Y$_2$O$_3$	2.61	1.37±0.15	-1.21	1.03	1.88	1.24±0.15	8.3	53±8
Y$_2$O$_{3,IL}$	2.52	1.46±0.19	-1.21	0.77	1.88	1.34±0.21	7.7	56±8

3.3 Film-substrate interface characteristics

Adhesion between the film and the substrate significantly impacts the mechanical performance and reliability of the thin-film coatings. Good adhesion will prevent delamination (flaking off) of the coatings which is desirable for long process reactor duty cycles. Here, we explored the role of the 14 nm Al$_2$O$_3$ interface layer for the film-substrate interface characteristics. Methods based on regular buckling (i.e. local delamination of the film from the substrate due to Poisson contraction) are available for quantification of film-substrate interface properties.[53] In our observations buckling occurred rarely, as a sign of excellent adhesion, but too irregularly for statistically meaningful analysis. Therefore, we quantified film-substrate interface quality from the crack count (number of

film cracks along a horizontal line in SEM field of view; e.g. Figure 3d) vs. tensile strain data (Figure S5) as follows. When the film remains fully attached to the substrate (as it does in our case; Figure 3e and 3f), the characteristic strain for interfacial decohesion propagating in the steady state (ε_{if}) can be equated to the total strain in the film at the onset of the saturation of the crack count ($\varepsilon_{sat} + \varepsilon_r{}^{Al}$):[54]

$$\varepsilon_{if} = \left(\frac{2\Gamma_{if}}{Eh}\right)^{1/2} = \varepsilon_{sat} + \varepsilon_r^{Al}. \tag{8}$$

This yields a lower bound for the film-substrate interface toughness Γ_{if}.[54] Owing to the statistical nature of the fragmentation process and consequently slowly saturating crack count vs. strain curve, the determination of ε_{sat} is somewhat ambiguous. Here, we have defined the ε_{sat} value as the strain that corresponds to a crack count 2 % below that at the maximum strain in the tensile experiment (Figure S5).

The obtained lower bound values of interface toughness for our film-substrate combinations fall in the range 27-56 J/m^2 (Table 2). The values for the NL1-NL3 films do not exhibit clear dependence on the layer structure, and therefore the interface toughness is primarily governed by the identical interface layers, rather than the differences in the total layer structure. Remarkably though, the values for the NL1-NL3 films are higher than that for the Al$_2$O$_3$ film. This seems to indicate that despite the identical potential for strong bonding between the film and the substrate from a chemical point of view, having a thin Al$_2$O$_3$ adhesion layer can yield higher interface toughness as compared to a thicker Al$_2$O$_3$ film. The data for the NL4 and Y$_2$O$_3$ indicate that the insertion of the Al$_2$O$_3$ interface layer—the native oxide material of the Al substrate—enables achieving higher interface toughness values. The interface toughness value for the Y$_2$O$_3$ film is higher than that for the Al$_2$O$_3$ film. This is surprising, as the adhesion of Al$_2$O$_3$ to Al as the natural/native oxide is expected to be

particularly strong,[55] even when compared to other native or non-native metal/oxide interfaces;[55-57] future work is required to understand this observation.

## *3.4 High-temperature measurements*

In applications protective coatings often must withstand elevated temperatures above room temperature. Elevated temperatures thermally expand the coatings and especially the underlying metal parts, such that thermal expansion mismatch induces thermal strain in the coatings. We probed briefly the high-temperature behavior of our Al_2O_3 coatings on Al substrate through tensile experiments accompanied with in-situ heating and in-situ optical microscopy (in room air). The chosen temperature (425 °C) is relevant for Al-based reactor tools; higher temperature processing e.g., in semiconductor manufacturing, then requires other base materials. In the following discussion we do not expect any coating crystallization as a result of our high temperature tensile test as it is well established in literature that ALD Al_2O_3 films only crystallize above 800-1000°C, independent of the deposition temperature.[11, 58-60]

The samples were first heated from room temperature to 425 °C (thermal tensile strain build up) and then additional uniaxial tensile strain was applied keeping the temperature constant. After completing the heating step and by applying additional tensile strain the films started to fracture at total strain values, i.e. COS values, of 2.36 % and 1.2 % for the 94-nm film and for the 500-nm film, respectively. These values follow reasonably well the known inverse-square-root film
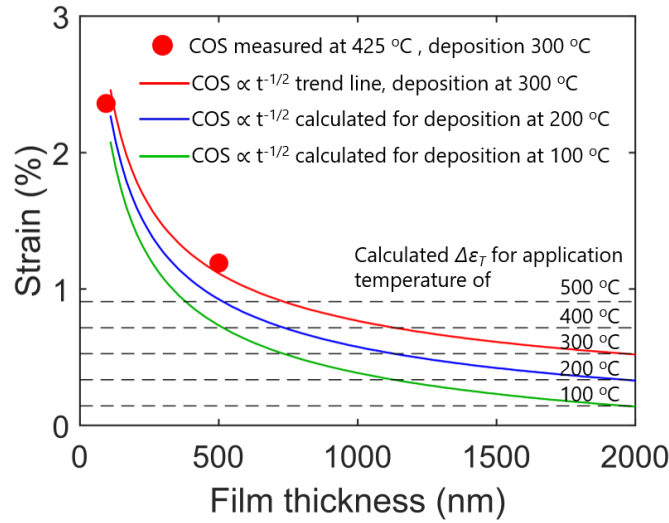
Figure 5. Measured high-temperature (425 °C) COS data for 94-nm and 500-nm Al₂O₃ films on Al substrate and extrapolation of the data following the inverse-square-root thickness dependence of COS. Also shown are calculated thickness dependencies of COS for lower (imaginary) deposition temperatures; the blue and the green curves are obtained by offsetting from the red one by 0.19 and 2*0.19 % (thermal strains corresponding to ΔT of 100 °C and 200 °C) The dashed horizontal lines represent the calculated thermal strain for a temperature increase from room temperature to a set of possible application temperatures. Crossing points of the COS curves and the horizontal thermal strain lines can be used to predict whether the coating would thermally crack in a given application and deposition temperatures for a given coating thickness.

thickness dependence of COS (Figure 5),[48] and hence the onset of fragmentation at 425 °C is primarily governed by the film properties, even though the Al substrate is approaching its melting point ($T/T_{melt} = 0.76$). We see that the high-temperature COS values are slightly higher than the room-temperature values (1.84% for 100 nm film and 0.9 % for the 500 nm film). This is reasonable, as the increased plasticity of the substrate at high temperature is expected to delay the fracture onset (yield stress ~ 20 MPa at ~ 400 °C).

We note that cracks due to thermal strain were not observed during the heating step, and additional tensile strain had to be applied to form cracks. The coatings therefore exhibit good tolerance for high temperatures, and for example for ~100 nm Al_2O_3 films, the strain tolerance (COS) of ~ 2 % would translate through equation (3) to tolerance of temperatures higher than the melting point of the Al substrate (Figure 6). Note also that the strain/temperature tolerance can be engineered through the choice of the deposition temperature. In our case the post-deposition cooling (from 300 °C to 25 °C) brings the films under compressive strain (ε_r^{Al} = -0.41 % for Al_2O_3, equation (4), Figures 4c and 6). Therefore, in applications, operating temperatures on the order of the film-deposition temperature would be needed for exerting a tensile strain state in the films. For example,
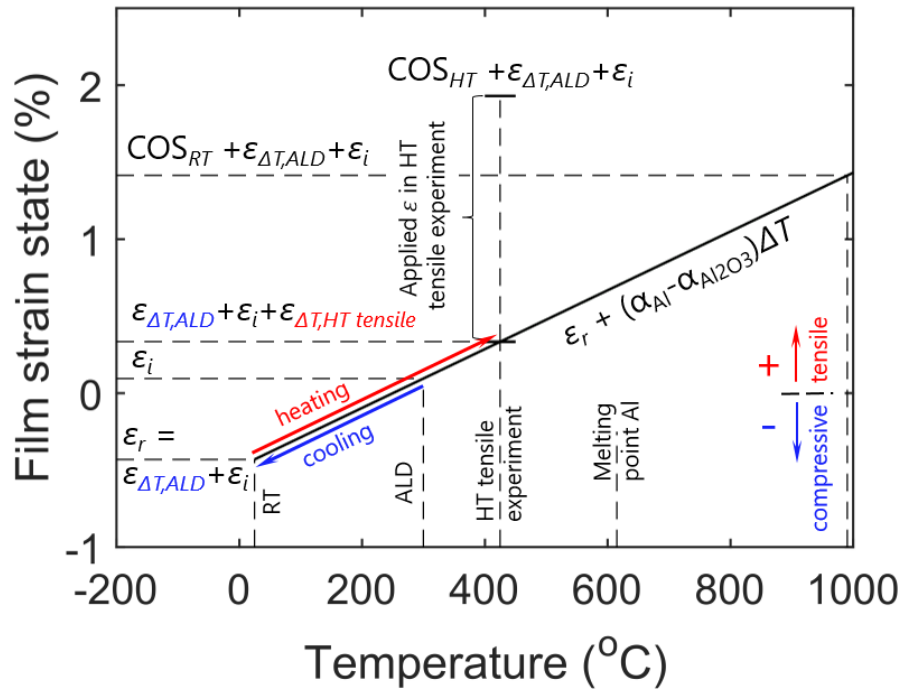
Figure 6. The strain state of the 94-nm Al_2O_3 film on the Al substrate as a function of temperature, in connection to the post-ALD cooling from 300 °C to room temperature (RT) and the subsequent heating step in the high-temperature (HT) tensile experiment. The strain (ε) indices r, i, and ΔT refer to the residual, intrinsic and thermal strain components of the Al_2O_3 film on the Al substrate. The strain levels corresponding to the measured room-temperature and high-temperature crack onset strain values corrected for the residual strain are shown for reference. Melting point of Al6061-T6 is also shown for reference; note that the melting point could vary for other Al alloys depending on the composition.

the temperature of 425 °C induces a thermal tensile strain ($\Delta T = 125$ °C) of 0.24 %, and accounting for the intrinsic tensile strain of 0.13 % (equations 2-4), the total strain at 425 °C is only moderately tensile of 0.33 %, well below what is needed to fracture the coating (Figure 6). Overall, strain/temperature tolerance deteriorates with increasing film thickness and decreasing deposition temperature, the former through the inverse square root dependence and the latter by reduction in the initial room-temperature compressive strain (by 0.19 % per deposition temperature decrease of 100 °C) as is depicted in Figure 5.

Elevated temperatures can facilitate fractureless interface sliding, seen as an increase in saturation crack spacing (λ).[21, 22, 61] We observe a substantial (five-fold) increase in λ for our Al_2O_3 films on Al when comparing the room-temperature data to the data taken at 425 °C ($T/T_{melt} = 0.76$; Figure 7), similar to the previously observed results for SiO_2 films on Cu substrate ($T/T_{melt} = 0.57$).[22] Interface sliding is facilitated by self-diffusion of metal atoms at low strain rates ($\dot{\varepsilon}$) and by dislocation slip at high strain rates;[22] for the SiO_2/Cu interface the transition between these sliding mechanisms takes place approximately at $\dot{\varepsilon} = 3.4 \times 10^{-4}$ s^{-1} for $T/T_{melt} > 0.5$.[22] Assuming that our material system behaves similarly to the SiO_2/Cu system, it could thus be that in our case ($\dot{\varepsilon}$ of 2.8×10^{-4} s^{-1} at $T/T_{melt} = 0.76$) the interface deformation is yet dominated by diffusion. Future work on $\dot{\varepsilon}$ and T dependence will be needed for ascertaining the deformation mechanism.

In the framework of tensile fragmentation testing, the sliding viscosity (μ') describes the ease of sliding as

$$1/\mu' = (\dot{\varepsilon}\lambda^2)/(8\sigma_{fract}h), \tag{9}$$

where σ_{frac} is the fracture stress and h is the film thickness.[21] We obtain $1/\mu'$ of 1.4 and 1.6×10^{-16} $ms^{-1}Pa^{-1}$ for the 94 and 500 nm films, respectively, values that are on the order of values reported for Al/Si interfaces ($1/\mu' \sim 10^{-16}$ $ms^{-1}Pa^{-1}$)[21, 61] and are clearly higher than those for the Cu/SiO_2 and $Al/MgAl_2O_4$ interfaces ($1/\mu' \sim 10^{-18}$-10^{-17} $ms^{-1}Pa^{-1}$)[21, 22], at similar $T/T_{melting}$. We approximate interface roughness of ~10 nm at most for our Al_2O_3/Al interfaces (TEM images, Figure S6), similar to the Al/Si interface with roughness of 18-174 nm.[61] Therefore, as μ' is also known to increase with increasing interface roughness for diffusionally accommodated sliding,[22] it is
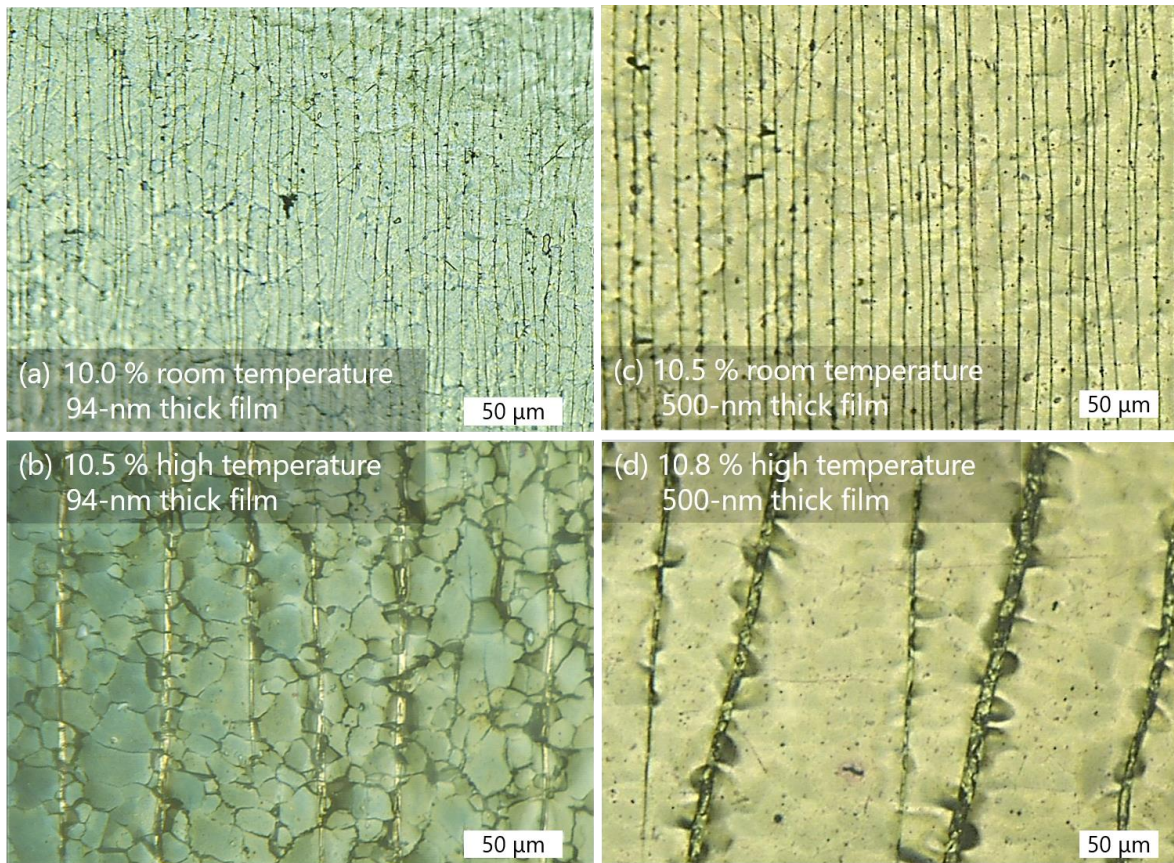
Figure 7. In-situ top-view optical microscope images of the surface of the Al_2O_3 films on the Al substrate after straining to around 10 % uniaxial tensile strain: the 94-nm-thick film strained (a) at room temperature and (b) at high temperature 425 ºC, the 500-nm film strained (c) at room temperature and (d) at high temperature 425 ºC. The grain boundaries (dark tone) of the underlying Al substrate are particularly visible in (b). The saturation crack spacing values are (a) 7.1 μm, (b) 42 μm, (c) 11.3 μm, and (d) 65 μm. Tensile strain acts in the horizontal direction, and the cracks are seen as vertical lines.

plausible that the low viscosity for our Al_2O_3/Al interfaces is driven by the reasonably low interface roughness.

4. Conclusions

In this work we studied the structural and mechanical properties of atomic layer deposited Al_2O_3, Y_2O_3 thin films and their nanolaminates on Al metal substrates for potential application as protective coatings for metallic components in harsh and corrosive environments. Through XRR and TEM we observed that Al_2O_3 and Y_2O_3 form well-defined layer structures even at sub-nanometer layer thickness. GIXRD and TEM indicate that Y_2O_3 layers have a strong tendency to crystallize, such that even at 6 nm layer thickness the Y_2O_3 layers are fully crystalline. Tuning the composition and layer structure enables tailoring the strain tolerance of the coatings with higher Al_2O_3 content, denser layer spacing and amorphization favoring higher crack onset strain, as is seen through uniaxial tensile straining experiments coupled with in-situ microscopy. Adhesion of the films to the substrate is qualitatively good as substantial delamination is absent in the tensile experiments, and moreover, the 14 nm Al_2O_3 interface layer (at the film/substrate interface) is found to enhance interface toughness. In view of the fragmentation onset, elevated temperatures ($\leq$ 425 °C) do not deteriorate the strain tolerance of the coatings on aluminum, and hence room-temperature data already provides us with a good indication of the high temperature behavior. The saturation crack spacing increases substantially at high temperatures, most likely due to the interface sliding mechanisms activating with the elevated temperature. The results are interesting for semiconductor manufacturing and other applications where metal parts/components require mechanically robust protective coatings. The present data provides a benchmark data for future studies on other substrate-films combinations in the field of increasing interest, yet at its infancy.

ASSOCIATED CONTENT

Supporting Information. Figure S1: Dimensions of the tensile samples. Figure S2: Electron diffraction pattern for the NL4 film. Figure S3: Comparison of the COS values based on optical and scanning electron microscopy. Figure S4: Top-view optical microscope images for the strained $NL4_{IL}$ film on a polyimide substrate. Figure S5: Crack count vs. strain curve for the interface toughness evaluation. Figure S6: A transmission electron microscope lamella of the $NL4_{IL}$ film on Al. Table S1: Elastic modulus, Poisson's ratio and thermal expansion coefficient values for the film materials.

AUTHOR INFORMATION

Corresponding Author

*barbara.putz@unileoben.ac.at

Author Contributions

The manuscript was written through contributions of all authors. All authors have given approval to the final version of the manuscript.

Present Address:

†Swiss Cluster AG, Feuerwerkerstrasse 39, Thun CH-3602, Switzerland

References

(1) Shih, H. In *A Systematic Study and Characterization of Advanced Corrosion Resistance Materials and Their Applications for Plasma Etching Processes in Semiconductor Silicon Wafer Fabrication;* Shih, H., Ed.; Corrosion Resistance; InTech: 2012; .

(2) Kim, D.; Lee, S.; Alexander, W. B.; Kim, K.; Oh, Y.; Lee, S. X-Ray Photoelectron Spectroscopy Study on the Interaction of Yttrium–Aluminum Oxide with Fluorine-Based Plasma. *J Am Ceram Soc* **2011***, 94*, 3455-3459.

(3) Matero, R.; Ritala, M.; Leskelä, M.; Salo, T.; Aromaa, J.; Forsén, O. Atomic layer deposited thin films for corrosion protection. *J. Phys. IV France* **1999***, 09*, Pr8-493-Pr8-499.

(4) Díaz, B.; Härkönen, E.; Świątowska, J.; Maurice, V.; Seyeux, A.; Marcus, P.; Ritala, M. Low-temperature atomic layer deposition of Al2O3 thin coatings for corrosion protection of steel: Surface and electrochemical analysis. *Corros. Sci.* **2011***, 53*, 2168-2175.

(5) Härkönen, E.; Díaz, B.; Świątowska, J.; Maurice, V.; Seyeux, A.; Vehkamäki, M.; Sajavaara, T.; Fenker, M.; Marcus, P.; Ritala, M. Corrosion Protection of Steel with Oxide Nanolaminates Grown by Atomic Layer Deposition. *J. Electrochem. Soc.* **2011***, 158*, C369.

(6) Marin, E.; Guzman, L.; Lanzutti, A.; Fedrizzi, L.; Saikkonen, M. Chemical and electrochemical characterization of hybrid PVD+ALD hard coatings on tool steel. *Electrochem. Commun.* **2009***, 11*, 2060-2063.

(7) Potts, S. E.; Schmalz, L.; Fenker, M.; Díaz, B.; Świątowska, J.; Maurice, V.; Seyeux, A.; Marcus, P.; Radnóczi, G.; Tóth, L.; Kessels, W. M. M. Ultra-Thin Aluminium Oxide Films Deposited by Plasma-Enhanced Atomic Layer Deposition for Corrosion Protection. *J. Electrochem. Soc.* **2011***, 158*, C132.

(8) Shan, C. X.; Hou, X.; Choy, K. Corrosion resistance of TiO2 films grown on stainless steel by atomic layer deposition. *Surf. Coat. Technol.* **2008***, 202*, 2399-2402.

(9) Shan, C. X.; Hou, X.; Choy, K.; Choquet, P. Improvement in corrosion resistance of CrN coated stainless steel by conformal TiO2 deposition. *Surf. Coat. Technol* **2008***, 202*, 2147-2151.

(10) Knez, M.; Nielsch, K.; Niinistö, L. Synthesis and surface engineering of complex nanostructures by atomic layer deposition. *Adv. Mater.* **2007***, 19*, 3425-3438.

(11) Miikkulainen, V.; Leskelä, M.; Ritala, M.; Puurunen, R. L. Crystallinity of inorganic films grown by atomic layer deposition: Overview and general trends. *J. Appl. Phys.* **2013***, 113*, 021301.

(12) Meng, X.; Yang, X.; Sun, X. Emerging Applications of Atomic Layer Deposition for Lithium-Ion Battery Studies. *Adv. Mater.* **2012***, 24*, 3589-3615.

(13) Piper, D. M.; Travis, J. J.; Young, M.; Son, S.; Kim, S. C.; Oh, K. H.; George, S. M.; Ban, C.; Lee, S. Reversible High-Capacity Si Nanocomposite Anodes for Lithium-ion Batteries Enabled by Molecular Layer Deposition. *Adv. Mater.* **2014**, *26*, 1596-1601.

(14) Melskens, J.; van de Loo, B. W. H.; Macco, B.; Black, L. E.; Smit, S.; Kessels, W. M. M. Passivating Contacts for Crystalline Silicon Solar Cells: From Concepts and Materials to Prospects. *IEEE Journal of Photovoltaics* **2018**, *8*, 373-388.

(15) Wang, H.; Zhao, Y.; Wang, Z.; Liu, Y.; Zhao, Z.; Xu, G.; Han, T.; Lee, J.; Chen, C.; Bao, D.; Huang, Y.; Duan, Y.; Yang, Y. Hermetic seal for perovskite solar cells: An improved plasma enhanced atomic layer deposition encapsulation. *Nano Energy* **2020**, *69*, 104375.

(16) Park, J.; Chae, H.; Chung, H. K.; Lee, S. I. Thin film encapsulation for flexible AM-OLED: a review. *Semicond. Sci. Technol* **2011**, *26*, 034001.

(17) Meyer, J.; Schneidenbach, D.; Winkler, T.; Hamwi, S.; Weimann, T.; Hinze, P.; Ammermann, S.; Johannes, H. -.; Riedl, T.; Kowalsky, W. Reliable thin film encapsulation for organic light emitting diodes grown by low-temperature atomic layer deposition. *Appl. Phys. Lett.* **2009**, *94*, 233305.

(18) Skoog, S. A.; Elam, J. W.; Narayan, R. J. Atomic layer deposition: medical and biological applications. *Int. Mater. Rev.* **2013**, *58*, 113-129.

(19) Nazarov, D. V.; Smirnov, V. M.; Zemtsova, E. G.; Yudintceva, N. M.; Shevtsov, M. A.; Valiev, R. Z. Enhanced Osseointegrative Properties of Ultra-Fine-Grained Titanium Implants Modified by Chemical Etching and Atomic Layer Deposition. *ACS Biomater. Sci. Eng.* **2018**, *4*, 3268-3281.

(20) Ruoho, M.; Niemelä, J. P.; Guerra-Nunez, C.; Tarasiuk, N.; Robertson, G.; Taylor, A. A.; Maeder, X.; Kapusta, C.; Michler, J.; Utke, I. Thin-Film Engineering of Mechanical Fragmentation Properties of Atomic-Layer-Deposited Metal Oxides. *Nanomaterials* **2020**, *10(3)*, 558.

(21) Singh, G.; Yu, Y.; Ernst, F.; Raj, R. Shear strength and sliding at a metal–ceramic (aluminum–spinel) interface at ambient and elevated temperatures. *Acta Mater.* **2007**, *55*, 3049-3057.

(22) Jobin, V. C.; Raj, R.; Phoenix, S. L. Rate effects in metal-ceramic interface sliding from the periodic film cracking technique. *Acta Metall. Mater.* **1992**, *40*, 2269-2280.

(23) Taylor, A. A.; Edlmayr, V.; Cordill, M. J.; Dehm, G. The effect of temperature and strain rate on the periodic cracking of amorphous AlxOy films on Cu. *Surf. Coat. Technol* **2011**, *206*, 1855-1859.

(24) Miller, D. C.; Foster, R. R.; Zhang, Y.; Jen, S.; Bertrand, J. A.; Lu, Z.; Seghete, D.; O'Patchen, J. L.; Yang, R.; Lee, Y.; George, S. M.; Dunn, M. L. The mechanical robustness of

atomic-layer- and molecular-layer-deposited coatings on polymer substrates. *J. Appl. Phys.* **2009**, *105*, 093527.

(25) Miller, D. C.; Foster, R. R.; Jen, S.; Bertrand, J. A.; Seghete, D.; Yoon, B.; Lee, Y.; George, S. M.; Dunn, M. L. Thermomechanical properties of aluminum alkoxide (alucone) films created using molecular layer deposition. *Acta Mater.* **2009**, *57*, 5083-5092.

(26) Niemelä, J.; Rohbeck, N.; Michler, J.; Utke, I. Molecular layer deposited alucone thin films from long-chain organic precursors: from brittle to ductile mechanical characteristics. *Dalton Trans.* **2020**, *49*, 10832-10838.

(27) Niemelä, J.; Philip, A.; Rohbeck, N.; Karppinen, M.; Michler, J.; Utke, I. Mechanics of Nanoscale ε-Fe2O3/Organic Superlattices toward Flexible Thin-Film Magnets. *ACS Appl. Nano Mater.* **2021**, *4*, 1692-1701.

(28) Philip, A.; Niemelä, J. P.; Tewari, G.; Putz, B.; Edwards, T.; Itoh, M.; Utke, I.; Karppinen, M. Flexible ε-Fe2O3-terephthalate thin-film magnets through ALD/MLD. *ACS Appl. Mater. Interfaces* **2020**, *12(19)*, 21912-21921.

(29) Chudoba, T.; Schwarzer, N.; Richter, F. Determination of elastic properties of thin films by indentation measurements with a spherical indenter. *Surf. Coat. Technol* **2000**, *127*, 9-17.

(30) Ylivaara, O. M. E.; Liu, X.; Kilpi, L.; Lyytinen, J.; Schneider, D.; Laitinen, M.; Julin, J.; Ali, S.; Sintonen, S.; Berdova, M.; Haimi, E.; Sajavaara, T.; Ronkainen, H.; Lipsanen, H.; Koskinen, J.; Hannula, S.; Puurunen, R. L. Aluminum oxide from trimethylaluminum and water by atomic layer deposition: The temperature dependence of residual stress, elastic modulus, hardness and adhesion. *Thin Solid Films* **2014**, *552*, 124-135.

(31) Palko, J. W.; Kriven, W. M.; Sinogeikin, S. V.; Bass, J. D.; Sayir, A. Elastic constants of yttria (Y2O3) monocrystals to high temperatures. *J. Appl. Phys.* **2001**, *89*, 7791-7796.

(32) Mishnaevsky, L. L. *Computational Mesomechanics of Composites: Numerical Analysis of the Effect of Microstructures of Composites of Strength and Damage Resistance*, 1 ed; John Wiley & Sons, Ltd: Chichester, West Sussex, England, 2007; .

(33) Daniel, I. M.; lshai, O. *Engineering Mechanics of Composite Materials*, 2nd ed; Oxford University Press: New York, 2006; .

(34) Schapery, R. A. Thermal Expansion Coefficients of Composite Materials Based on Energy Principles. *J. Composite Mater.* **1968**, *2*, 380-404.

(35) Kirfel, A.; Eichhorn, K. Accurate structure analysis with synchrotron radiation. The electron density in Al2O3 and Cu2O. *Acta Cryst.* **1990**, *A46*, 271-284.

(36) Klein, P. H.; Croft, W. J. Thermal Conductivity, Diffusivity, and Expansion of Y2O3, Y3 Al5O12, and LaF3 in the Range 77°–300°K. *J. Appl. Phys.* **1967**, *38*, 1603-1607.

(37) Potts, S. E.; Keuning, W.; Langereis, E.; Dingemans, G.; van de Sanden, M. C. M.; Kessels, W. M. M. Low Temperature Plasma-Enhanced Atomic Layer Deposition of Metal Oxide Thin Films. *J. Electrochem. Soc.* **2010**, *157*, P66.

(38) Barbos, C.; Blanc-Pelissier, D.; Fave, A.; Botella, C.; Regreny, P.; Grenet, G.; Blanquet, E.; Crisci, A.; Lemiti, M. Al2O3 thin films deposited by thermal atomic layer deposition: Characterization for photovoltaic applications. *Thin Solid Films* **2016**, *617*, 108-113.

(39) Barbos, C.; Blanc-Pelissier, D.; Fave, A.; Botella, C.; Regreny, P.; Grenet, G.; Blanquet, E.; Crisci, A.; Lemiti, M. Al2O3 thin films deposited by thermal atomic layer deposition: Characterization for photovoltaic applications. *Thin Solid Films* **2016**, *617*, 108-113.

(40) Lee, B. H.; Yoon, B.; Anderson, V. R.; George, S. M. Alucone Alloys with Tunable Properties Using Alucone Molecular Layer Deposition and Al_2O_3 Atomic Layer Deposition. *J. Phys. Chem. C* **2012**, *116*, 3250-3257.

(41) Abdulagatov, A. I.; Amashaev, R. R.; Ashurbekova, K. N.; Ramazanov, S. M.; Palchaev, D. K.; Maksumova, A. M.; Rabadanov, M. K.; Abdulagatov, I. M. Atomic Layer Deposition of Y_2O_3 Using Tris(butylcyclopentadienyl)yttrium and Water. *Russ. Microelectron.* **2019**, *48(1)*, 1-12.

(42) Boysen, N.; Zanders, D.; Berning, T.; Beer, S. M. J.; Rogalla, D.; Bock, C.; Devi, A. Atomic layer deposition of dielectric Y2O3 thin films from a homoleptic yttrium formamidinate precursor and water. *RSC Adv.* **2021**, *11*, 2565-2574.

(43) Århammar, C.; Pietzsch, A.; Bock, N.; Holmström, E.; Araujo, C. M.; Gråsjö, J.; Zhao, S.; Green, S.; Peery, T.; Hennies, F.; Amerioun, S.; Föhlisch, A.; Schlappa, J.; Schmitt, T.; Strocov, V. N.; Niklasson, G. A.; Wallace, D. C.; Rubensson, J.; Johansson, B.; Ahuja, R. Unveiling the complex electronic structure of amorphous metal oxides. *Proc. Natl. Acad. Sci. USA* **2011**, *108*, 6355.

(44) Chawla, V.; Ruoho, M.; Weber, M.; Chaaya, A. A.; Taylor, A. A.; Charmette, C.; Miele, P.; Bechelany, M.; Michler, J.; Utke, I. Fracture Mechanics and Oxygen Gas Barrier Properties of Al2O3/ZnO Nanolaminates on PET Deposited by Atomic Layer Deposition. *Nanomaterials* **2019**, *9*, 88.

(45) Romano Brandt, L.; Salvati, E.; Bourhis, E. L.; Korsunsky, A. M. Mode I fracture toughness determination in Cu/W nano-multilayers on polymer substrate by SEM - Digital Image Correlation. *J. Mech. Phys. Solids* **2020**, *145*, 104145.

(46) Cardinali, V.; Marmois, E.; Le Garrec, B.; Bourdet, G. Determination of the thermo-optic coefficient dn/dT of ytterbium doped ceramics (Sc2O3, Y2O3, Lu2O3, YAG), crystals (YAG, CaF2) and neodymium doped phosphate glass at cryogenic temperature. *Opt. Mater.* **2012**, *34*, 990-994.

(47) Taylor, A. A.; Edlmayr, V.; Cordill, M. J.; Dehm, G. The effect of film thickness variations in periodic cracking: Analysis and experiments. *Surf. Coat. Technol* **2011**, *206*, 1830-1836.

(48) Leterrier, Y.; Andersons, J.; Pitton, Y.; Månson, J. A. E. Adhesion of silicon oxide layers on poly(ethylene terephthalate). II: Effect of coating thickness on adhesive and cohesive strengths. *J. Polym. Sci. B Polym. Phys.* **1997***, 35*, 1463-1472.

(49) Ahmed, F.; Bayerlein, K.; Rosiwal, S. M.; Göken, M.; Durst, K. Stress evolution and cracking of crystalline diamond thin films on ductile titanium substrate: Analysis by micro-Raman spectroscopy and analytical modelling. *Acta Materialia* **2011***, 59*, 5422-5433.

(50) Beuth, J. L. Cracking of thin bonded films in residual tension. *Int. J. Solids Structures* **1992***, 29*, 1657-1675.

(51) Lipomi, D. J.; Chong, H.; Vosgueritchian, M.; Mei, J.; Bao, Z. Toward mechanically robust and intrinsically stretchable organic solar cells: Evolution of photovoltaic properties with tensile strain. *Sol. Energy Mater Sol. Cells* **2012***, 107*, 355-365.

(52) Sawyer, E. J.; Zaretski, A. V.; Printz, A. D.; de los Santos, N. V.; Bautista-Gutierrez, A.; Lipomi, D. J. Large increase in stretchability of organic electronic materials by encapsulation. *Extreme Mech. Lett* **2016***, 8*, 78-87.

(53) Cordill, M. J.; Fischer, F. D.; Rammerstorfer, F. G.; Dehm, G. Adhesion energies of Cr thin films on polyimide determined from buckling: Experiment and model. *Acta Mater.* **2010***, 58 (16)*, 5520-5531.

(54) Wang, J. S.; Sugimura, Y.; Evans, A. G.; Tredway, W. K. The mechanical performance of DLC films on steel substrates. *Thin Solid Films* **1998***, 325*, 163-174.

(55) Siegel, D. J.; Hector, L. G.; Adams, J. B. Ab initio study of Al-ceramic interfacial adhesion. *Phys. Rev. B* **2003***, 67*, 092105.

(56) Muktepavela, F.; Bakradze, G.; Tamanis, E.; Stolyarova, S.; Zaporina, N. Influence of mechanoactivation on the adhesion and mechanical properties of metal/oxide interfaces. *phys. stat. sol. (c)* **2005***, 2*, 339-342.

(57) Zhang, W.; Smith, J. R. Nonstoichiometric Interfaces and Al2O3 Adhesion with Al and Ag. *Phys. Rev. Lett.* **2000***, 85*, 3225-3228.

(58) Zhang, L.; Jiang, H. C.; Liu, C.; Dong, J. W.; Chow, P. **Annealing of Al2O3 thin films prepared by atomic layer deposition**. *J. Phys. D: Appl. Phys.* **2007***, 40*, 3707.

(59) Jakschik, S.; Schroeder, U.; Hecht, T.; Gutsche, M.; Seidl, H.; Bartha, J. W. Crystallization behavior of thin ALD-Al2O3 films. *Thin Solid Films* **2003***, 425*, 216-220.

(60) Krautheim, G.; Hecht, T.; Jakschik, S.; Schröder, U.; Zahn, W. Mechanical stress in ALD-Al2O3 films. *Appl. Surf. Sci.* **2005***, 252*, 200-204.

(61) Peterson, K. A.; Dutta, I.; Chen, M. W. Diffusionally accommodated interfacial sliding in metal-silicon systems. *Acta Mater.* **2003***, 51*, 2831-2846.